

NUMERICAL ANALYSIS OF INTERACTION NOISE BETWEEN MAIN ROTOR AND TAIL ROTOR OF HELICOPTER

Choongmo YANG, Takashi AOYAMA, and Shigeru SAITO*
*Japan Aerospace Exploration Agency (JAXA)

Keywords: *main-rotor/tail-rotor interaction, CFD, interaction noise, overlapped grid system*

Abstract

Unsteady calculation of the interaction between tail-rotor and main-rotor wake of helicopter is conducted using an overlapped grid method. A moving overlapped grid system is used with three types of grid including rotor grid, inner background grid and outer background grid for helicopter flight simulation. The rotor grid, consisting of 2 blades for main-rotor and 4 blades for tail-rotor, communicates with inner-/outer-background grids during unsteady computations. The Blade-Vortex Interaction (BVI) noise of main-rotor and tail-rotor noise are predicted using a combination method of an unsteady Euler code with an aeroacoustic code based on the Ffowcs-Williams and Hawkings formulation. The effect of tail-rotor onto main-rotor and the tail-rotor noise are studied for the helicopter operating conditions.

1 General Introduction

There are several kinds of noise sources in helicopter as shown in Fig. 1. Among these noises, rotor noises including main rotor and tail-rotor are of interest in the fields of aerodynamics and aeroacoustics. Although the tail-rotor noise is a significant contributor to the excess noise that causes early detection and gives raise to the annoyance characteristics of helicopter, less effort have been directed towards understanding and reducing this noise source from tail-rotor^[1].

Many researches have been conducted to study tail-rotor characteristics. Chou^[2] showed that the main-rotor turbulent wake is one of the

most important source of tail-rotor broadband noise. Due to the size difference, isolated tail-rotor noise is known to be less important than the much louder main-rotor noise. However, the inflow turbulence noise from a tail-rotor can be very significant because it is operated in a highly turbulent environment, ingesting wakes from upstream components of the helicopter.

Also experimental researches have been conducted to obtain acoustic measurements to study not only the isolated tail-rotor^[3-5] but also main-rotor/tail-rotor interaction^[6]. However, the interaction noise between main-rotor and tail-rotor, which is one of the most significant noise sources in helicopter, was not investigated enough on account of its complicated operating condition and aerodynamic environment as well as the needs of huge computing resource. Most of the studies are focused on loading or thickness noise of tail-rotor^[7], and the interaction characteristics of tail-rotor are simplified for limited cases^[8].

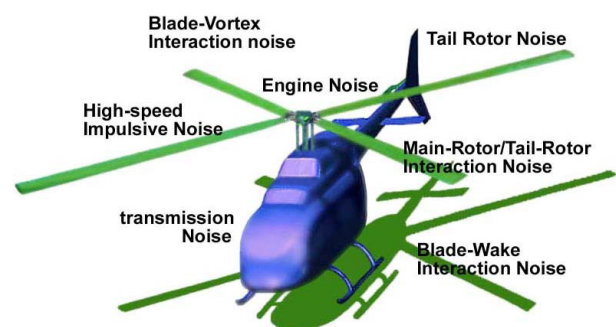


Fig. 1: Diagram of noise sources in helicopter

Interaction noise between tail-rotor and tip vortex of main-rotor becomes considerably

equal to main-rotor BVI noise according to flight condition, specially in the case of approaching flight when tip vortex from main-rotor collide with tail-rotor directly at the high rotation speed. Figure 2 shows tip vortex trajectories of main rotor during hover and forward flight. The effect of tip vortex onto tail rotor has a wide range of interaction condition according to the flight condition, the location of tail rotor, and operating condition.

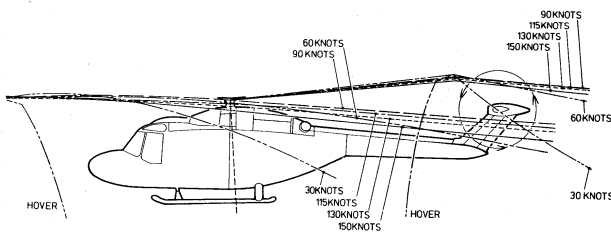


Fig. 2: Tip vortex trajectories during hover and forward flight^[9]

In this paper, unsteady calculation of an interaction between tail-rotor and tip vortex from main-rotor is conducted using an Euler code. A overlapped grid system is constructed for three types of grid including moving rotor grid, inner background grid and outer background grid. The rotor grid, consisting of main-rotor with 2 blades and tail-rotor with 4 blades, communicates with background grids during unsteady computations. The results include the characteristics of the fluctuating flow patterns for actual helicopter flight. Iso-surfaces of vorticity for various calculating conditions are compared to show the tip vortex movement and the effect of tail-rotor in hovering and forward flight conditions for main-rotor/tail-rotor configuration. Also the main-rotor/tail-rotor noise is predicted using a combination method of an unsteady Euler code with an aeroacoustic code based on the Ffowcs-Williams and Hawkings formulation.

The main objective of this research work is to develop the CFD method for full helicopter calculation with main-rotor and tail-rotor. This paper is focused on the tail-rotor noise calculation including tail-rotor self noise and the interaction noise with the main rotor wake.

2 Numerical Methods

2.1 Overlapped Grid System

A moving overlapped grid system with three different types of grids (rotor grid, inner and outer background grids) is used to simulate BVI of helicopter. Figure 3 shows a perspective view of grid system for the whole computational domain of grid system. The inner background grid is placed around the rotor disk. The outer background grid covers the whole computation region with a sparse grid density. The flow data are exchanged between the inner and outer background grids, and between rotor grid and inner-background grid. The body-fitted blade grid in O-H topology moves along with the blade motion including rotation, flapping, feathering, and lagging.

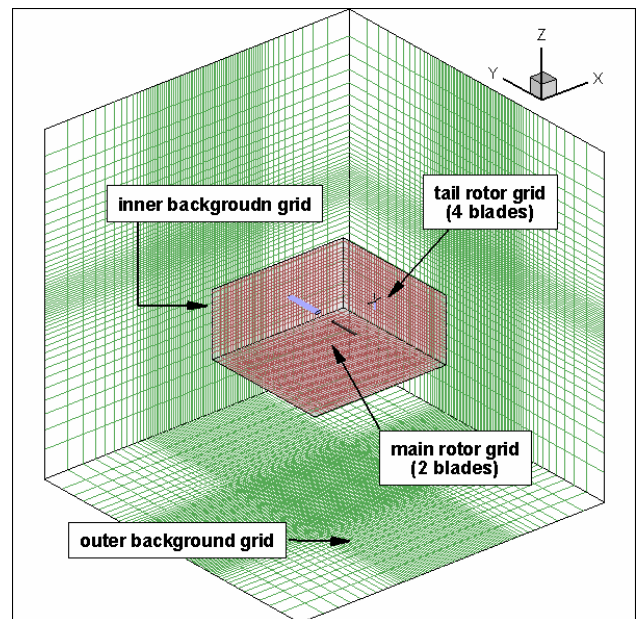


Fig.3: Perspective view of grid system

Figure 4 shows the geometric dimensions for each grid. Figure 4(a) shows the geometric dimension of two background grids. The airfoil model of main-rotor blade comes from AH1-OLS blade^[10] (modified BHT 540), which has been used for the aerodynamic and noise testing by NASA. The characteristics of OLS rotor with 1.916m diameter (6.6ft) are shown in Fig. 4(b). The aspect ratio of main-rotor is 9.21. The rotor

motion is also set to be one of the test cases of NASA experiment.

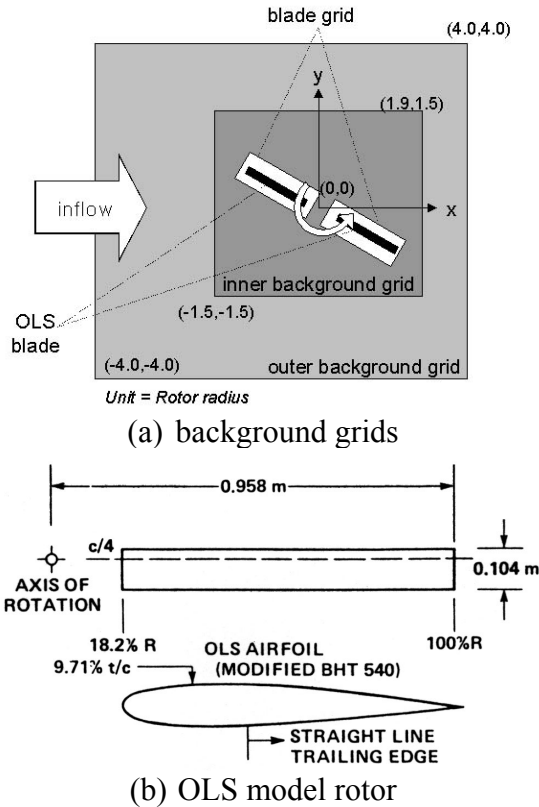


Fig.4: Geometric dimension of computation

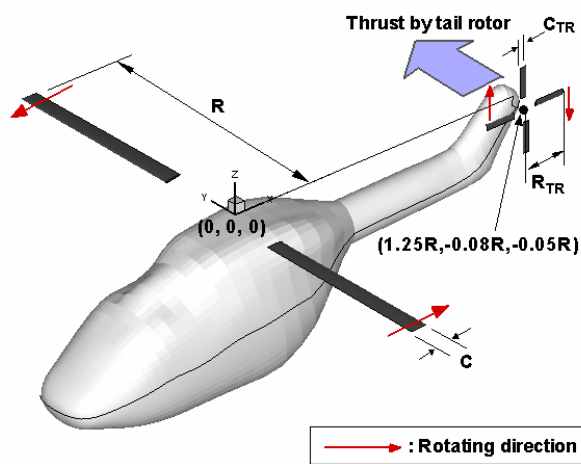


Fig.5: Geometric dimension of main/tail rotors

Figure 5 illustrates the relative position of tail rotor and geometric specifications of each rotor. The tail-rotor is pusher type producing thrust to the other side of tail-rotor location. The airfoil model of tail-rotor blade is NACA0012, and the angle of attack is 5° without twist angle. The

radius of tail-rotor is $1/6$ of that of main-rotor, and the aspect ratio of tail-rotor is 7.0.

Table 1 shows the specification of each grid. Most of the grid is concentrated in inner-background grid, which captures the trace of tip vortex during several rotations around rotor disk. The number of grid points in span-wise direction is considerably increased to match the grid density of the blade grid with that of the inner background grid. The grid spacing of the inner background grid corresponds to $0.1c$, where c is the chord length.

Table 1: Specifications of grid systems

Grid	
Inner Background grid	$(x \times y \times z)$ $450 \times 400 \times 80 = 14,400,000$
Outer Background grid	$(x \times y \times z)$ $83 \times 79 \times 49 = 321,293$
Main-rotor grid	$(\text{chord} \times \text{normal} \times \text{span}) \times \text{blade}$ $(77 \times 20 \times 70) \times 2 = 215,600$
Tail-rotor grid	$(\text{chord} \times \text{normal} \times \text{span}) \times \text{blade}$ $(77 \times 20 \times 55) \times 4 = 338,800$
Total	15,275,693 points
Spacing of inner background Grid	$0.1c (= 0.005R)$

2.2 Numerical Schemes

A three-dimensional numerical flow solver for the compressible Euler equation is used to analyze the detailed behavior of tip vortex^[11].

For the blade calculation, inviscid flux vectors are separated using Roe's flux difference splitting (FDS) algorithm^[12], where flux difference across a cell interface is divided into components associated with each characteristic wave with third-order accuracy using a TVD scheme. TVD scheme is known to be good in capturing shock wave without adding artificial dissipation. Since Roe's approximate Riemann solver does not have the consistency with the entropy condition and thus permits physically inadmissible expansion shock, an entropy correction is applied to resolve this inconvenience. For the time integration, second-order Euler backward scheme is used in the conventional delta form. A diagonalized ADI method with an upwind flux-split technique is used in the linearized implicit part for the

discretionary governing equations. A detailed derivation of the governing equation and numerical schemes is described in a previous work by Aoyama et al. [13].

The accuracy of this solver is second order in space and first order in time, respectively. In order to obtain the unsteady solution in forward flight conditions, the Newton iterative method with for iterations is used at each time step. The typical dividing number along the azimuthal direction is about 4800 per revolution, which corresponds azimuth angles about 0.075° . The unsteady calculation is impulsively started from the azimuth angle of 0° . From the previous research, the starting vortex can be negligible in forward flight calculation. For the fixed wing calculation, the same numerical scheme is used for a single blade.

For the calculations over background grid, the flux difference across cell interface is divided also using a compact TVD scheme^[14] to get third order accuracy. MUSCL cell interface value is modified to achieve 4th-order high accuracy in the background Cartesian grid. Simple High-resolution Upwind Scheme (SHUS)^[15] is employed to obtain numerical flux. SHUS is one of the Advection Upstream Splitting Method (AUSM) type approximate Riemann solvers and has small numerical diffusion. The four stage Runge-Kutta method is used for the present calculation. The free stream condition is applied for the outer boundary of the outer background grid.

In this study, calculations are performed using Central Numerical Simulation System (CeNSS), the main part of the third-generation numerical simulator of JAXA. It is composed of high performance UNIX servers, FUJITSU PRIMEPOWER, which are connected by a crossbar network. CeNSS has 9TFLOPS peak performance, 3TB memory, 50TB disk storage, and 600TB tape archive. It takes about 100 hours to obtain a fully converged solution of a rotor Euler calculation with about 15 million grid points using 36CPUs.

2.3 Noise Calculation Using Ffowcs-Williams and Hawkings Formulation

The prediction method of the far field acoustic pressure is based on the combination of CFD technique with an acoustic equation solver. Although direct computation can be used to get the noise solution directly from the flow calculation with CFD based methods, this is available only in the near field in spite of huge computing cost. At present, the best way is the coupling with the integral method for far-field prediction. Acoustic analogy, which is rearranged into the Ffowcs Williams-Hawkings Equation, is widely used and still under construction for better applications. Retarded time solution to the Ffowcs-Williams and Hawkings equation, neglecting quadruple noise, can be written in the form of Formulation1 by Farassat^[16]. The prediction of rotor noise is conducted in the following procedures: 1) calculation of sound pressure of the noise source, 2) acoustic prediction computation at the observer position, and 3) post-processing of the noise data in the way of sound level using visualization or audible converting.

Hypothesis of the Ffowcs-Williams and Hawkings equation^[17] to be satisfied are known that the noise source must lay in low speed flow, and the observer should be located outside of the source region (i.e. outside of the boundary layer, separation flow or wake) in order to avoid the nonlinear effect. In most calculations to compare the results with wind tunnel experiment, the observer moves in the same direction and at the same speed as the noise source. The pressure distribution on the blade surface calculated by the CFD code is stored every 0.5 degrees in azimuth-wise direction as the input data in noise calculation.

3 Results and Discussion

3.1 Conditions and Validation

Numerical computations are performed by the present method for the realistic rotor system, which was tested in the anechoic Deutsch-Niederlaendischer Windkanal (DNW). Acoustic data have documented the BVI impulsive noise radiated from a 1/7-scale model main rotor of

AH-1 series helicopter. The dynamic blade motions such as flapping, feathering, and lagging are defined by the input data. These input data can include azimuth-wise data or 1st harmonic function obtained by CAMRADII (Comprehensive Analytical Code for Rotorcraft Aerodynamics and Dynamics) [18]. The inertial forces by these dynamic motions have not considered yet in the present calculations.

One of the testing conditions is selected to evaluate the capability of our code to predict BVI noise. The dimension of the calculated rotor and the operating conditions are summarized in Tables 2. The shaft tilt angles are corrected by the Heyson's method [19].

Table 2: Operating conditions

Main-rotor	
Tip Mach Number, M_T	0.664
Advance ratio, μ	0.164
Tip path plane angle	3.0°
Collective pitch angle, θ_0	5.20°
Cyclic pitch angle, θ_c	-1.33°
Cyclic pitch angle, θ_s	2.72°

Figure 6 shows one of the microphone positions in the experiment, where high BVI noise can be measured. Sound pressure is calculated at this position from blade surface pressure using the aeroacoustic code based on the FW-H formulation.

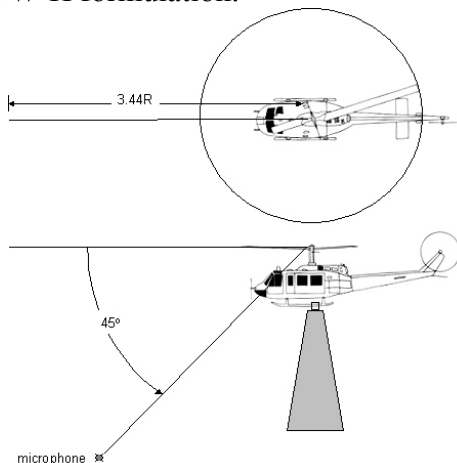


Fig. 6: Microphone position

Figure 7 shows the comparison of sound pressure histories between measurement and calculation for one revolution of rotor blade.

The calculated sound pressure waveform of BVI noise clearly shows distinct spikes caused by the interactions between blades and vortices. The higher accuracy numerical schemes and very large-scale computation lead us to these satisfying results. Even the peak values show some discrepancy in magnitude, the calculation shows good agreement in the peak position. It implies that the calculation can predict the BVI phenomena, which is characterized by the peak of sound pressure.

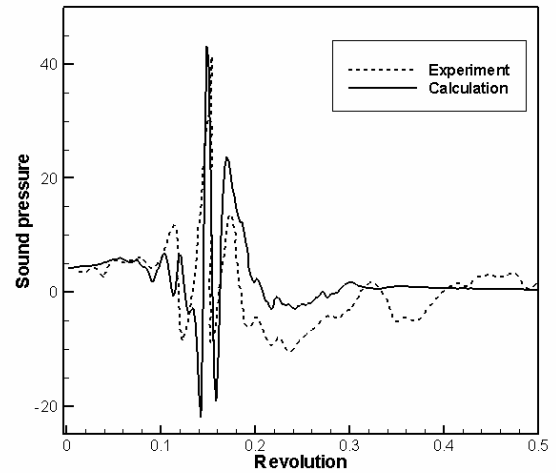


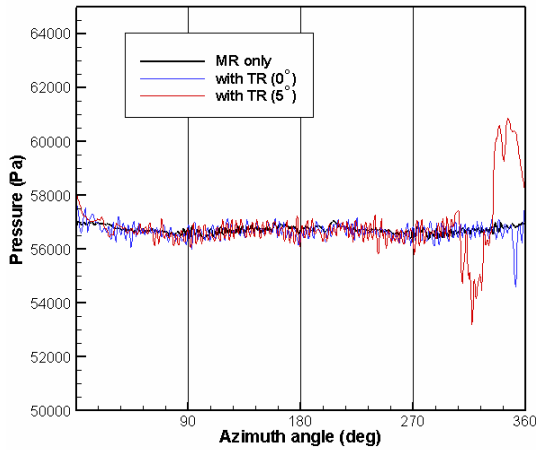
Fig. 7: Comparison of sound pressure between calculation and measurement

3.2 Hovering Flight

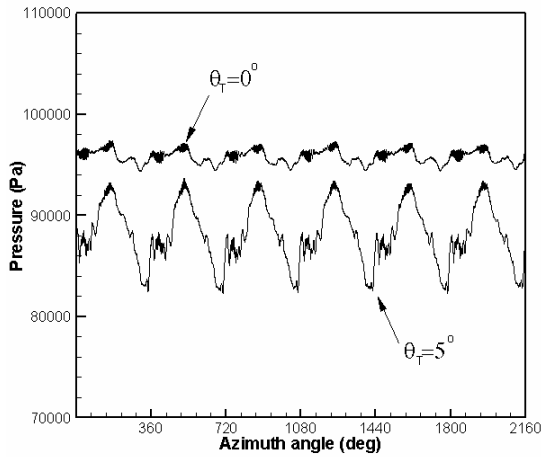
Hovering flight of helicopter is simulated to analyze tail-rotor effect without interference by the tip vortex of main-rotor. The angle of attack of tail-rotor, θ_T , is set to be 0° (non-lifting case) and 5° (lifting case). Table 3 shows the operating conditions for main-rotor and tail-rotor in hovering flight.

Table 3: Operating conditions

Main-rotor	
Tip Mach Number, M_M	0.664
Advance ratio, μ	0.164
Tip path plane angle	0.0°
Collective pitch angle, $\theta_{0,M}$	0.0°
Cyclic pitch angle, $\theta_{c,M}$ $\theta_{s,M}$	0.0°
Tail-rotor	
Tip Mach Number, M_T	0.664
Rotation ratio w.r.t. main-rotor	6.0
Geometric ratio w.r.t. main-rotor	1/6



(a) main-rotor



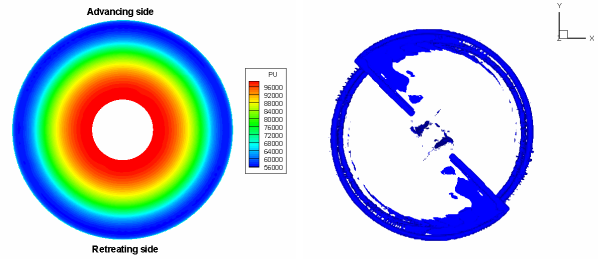
(b) tail-rotor

Fig.8: Pressure history at a point

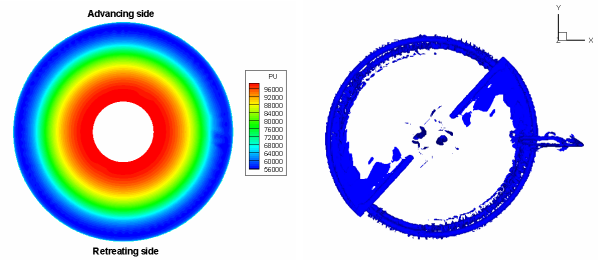
Figure 8 shows a pressure history of main-rotor(upper) and tail-rotor(lower) at one typical point on the upper surface (90% of span, 3 % of chord) in hovering flight during one revolution. Compared to the almost flat line of main-rotor only case (black line), the presence of tail-rotor (blue line and red line) disturbed the pressure at the end of the revolution of main rotor. Considering pressure histories of tail-rotor, the lifting tail-rotor shows a larger oscillation than the non-lifting case.

The effect of tail-rotor is also shown in Fig. 9, pressure carpets and vorticity iso-surfaces at top view of main-rotor disk. Pressure carpets are drawn by the pressure at one line on the upper surface (3 % of chord) during one revolution in hovering flight. As shown in vorticity iso-surfaces, the tip vortex from lifting tail-rotor is drawn into the tip vortex of main-rotor by the

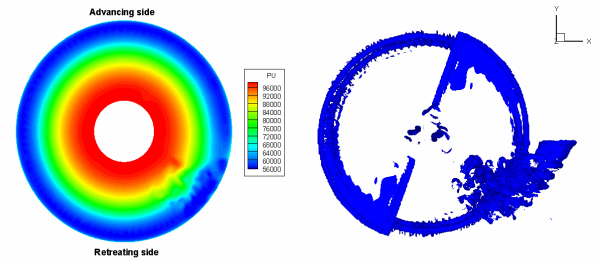
induced flow of hovering main-rotor. This tip vortex from tail-rotor disturbs the main-rotor around $300^\circ \sim 330^\circ$ azimuth angle, which also appears in the previous figure of pressure history of main-rotor.



(a) main-rotor only



(b) with non-lifting tail-rotor



(c) with lifting tail-rotor

Fig.9: Pressure carpet and vorticity iso-surface at top view of main-rotor

3.3 Forward Flight

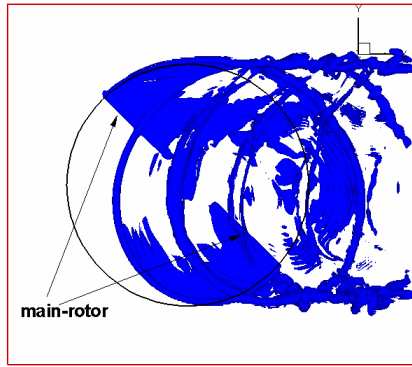
Forward flight of helicopter is simulated to analyze tail-rotor noise interfered by the tip vortex of main-rotor. The angle of attack of tail-rotor is also set to be 0° (non-lifting case) and 5° (lifting case). Table 4 shows the operating conditions for main-rotor and tail-rotor in forward flight.

Figure 10 shows the iso-surface of vorticity in the inner background grid at top view for main-rotor with/without tail-rotor. The vorticity surface shows the presence of main-rotor and tail-rotor as well as tip vortex from main-rotor in the first figure. The addition of tail-rotor

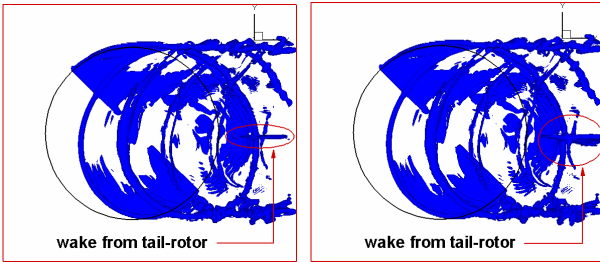
alters the vorticity surface in the next figures to show the effect of tail-rotor clearly.

Table 4: Operating conditions

Main-rotor	
Tip Mach Number, M_M	0.664
Advance ratio, μ	0.164
Tip path plane angle	3.0°
Collective pitch angle, $\theta_{0,M}$	5.2°
Cyclic pitch angle, $\theta_{c,M}$	-1.33°
Cyclic pitch angle, $\theta_{s,M}$	2.72°
Tail-rotor	
Tip Mach Number, M_T	0.664
Rotation ratio w.r.t. main-rotor	6.0
Geometric ratio w.r.t. main-rotor	1/6



(a) MR only



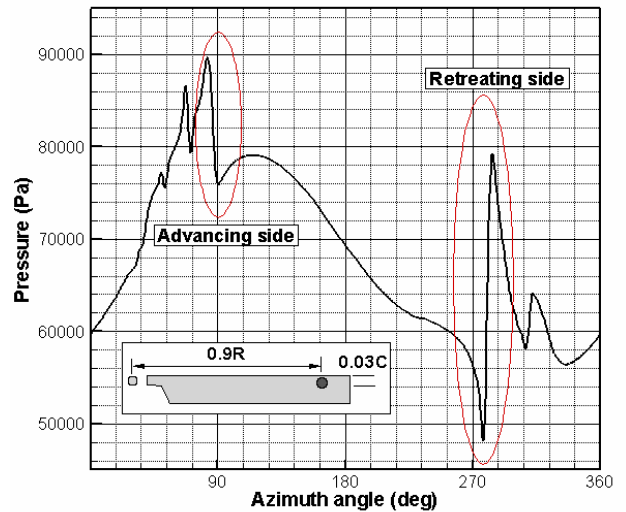
(b) with TR (0°)

(c) with TR (5°)

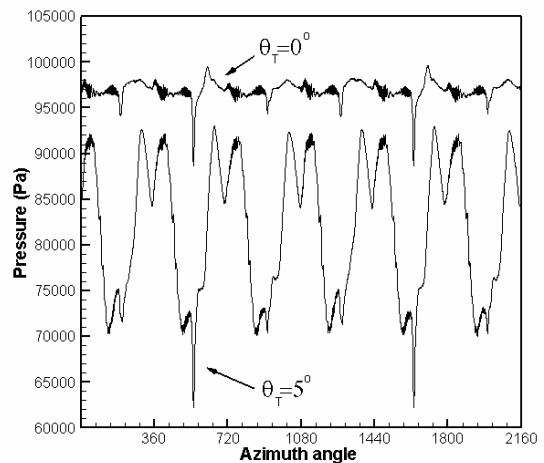
Fig.10: Iso-surface vorticity at top view

Figure 11 shows a pressure history of main-rotor and tail-rotor at one typical point on the upper surface (90% of span, 3 % of chord) in forward flight. As shown in Fig. 11(a), main-rotor experiences BVI around 85° and 280° of azimuth angle, which comes into view as sudden peaks of pressure. And the presence of tail-rotor seems negligible on the pressure history of main rotor. According to the rotation ratio between main-rotor and tail-rotor, tail rotor rotates six times during one revolution of main

rotor. For the non-lifting tail-rotor (0°), relatively small change is shown in oscillation amplitude of pressure compared to the lifting tail-rotor (5°). In both cases, the effect of the interaction with tip vortex from main-rotor appears as the peak around 540° (in 2nd revolution) and 1620° (in 5th revolution). Although the peak positions happen to be quite regular (periodic) in this flight condition, it should be mentioned that the interval of these interaction peaks are dependent on many parameters, such as forward velocity, rotation speed of tail-rotor, and number of blade in tail-rotor.



(a) main-rotor

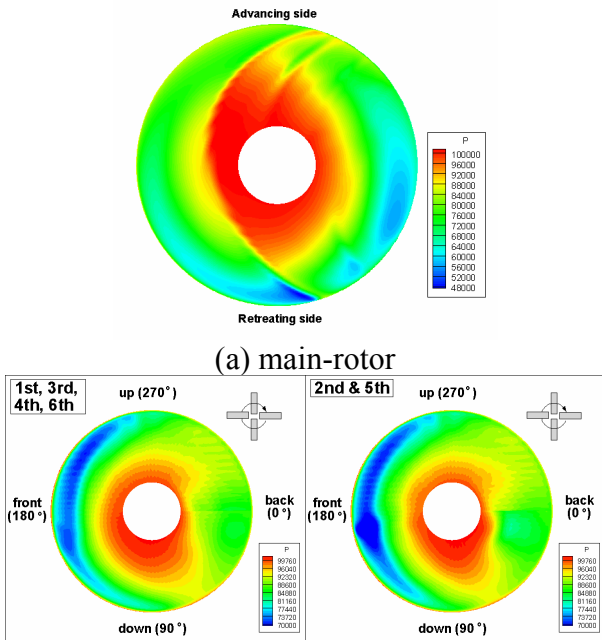


(b) tail rotor

Fig. 11: Time history of pressure at one point on upper surface for main-rotor and tail-rotor

Figure 12 shows pressure carpets of main-rotor disk and tail-rotor disks which are drawn

by the pressure at one typical line on the upper surface (3 % of chord) in forward flight. As tail-rotor happens to experience quite periodic pressure oscillation as shown in the previous figure, the pressure carpets during 1st, 3rd, 4th and 6th revolution are similar, and those during 2nd and 5th are almost identical among totally 6 revolutions, which are corresponding to one revolution of main-rotor. From the pressure carpet during 2nd revolution, we can easily find the interacting point with main-rotor wake at the highlighted area around 180° of tail-rotor azimuth angle, which coincides with the previous result.



(a) main-rotor
 (b) tail-rotor during 1st and 2nd revolution
 Fig.12: Pressure carpets of main-rotor and tail-rotor during one revolution

Another convenient way to understand the noise radiation of helicopter is using a hemispherical surface whose center is located at the origin of main-rotor (or helicopter) as shown in Fig. 13. A point on the hemispherical surface is specified by the radius, r , the azimuth angle, ψ , and the elevation angle, φ . The azimuth angle follows the count-clockwise main-rotor rotation when viewed from above. Elevation angle is defined as a negative value downward from the tip-path plane of the main-rotor. The contour values on the hemispherical surface represent

the peak sound pressure which is radiated from the main-rotor during one revolution at the distance of $r/R=1000$. Comparing three peak noise level contours, the peak positions are same ($\psi=205^\circ$, $\varphi=-25^\circ$) regardless of the tail-rotor conditions, which implies that the effect of tail-rotor is negligible when BVI happens.

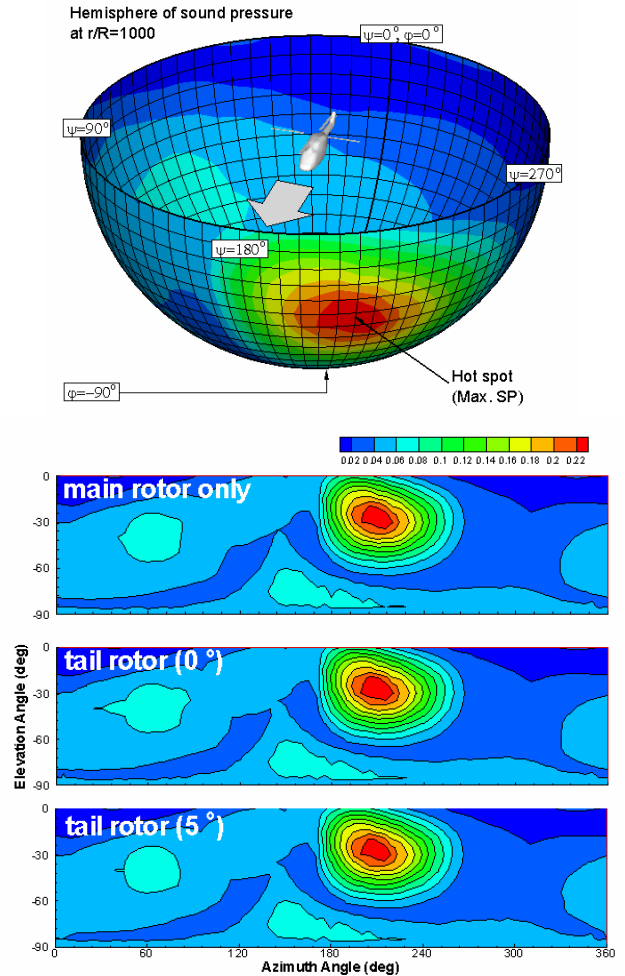


Fig.13: Peak noise contours for BVI

Table 5: Peak noise positions and values

case	ψ	φ	SP(Pa)
MR only	205°	-25°	0.2380
with TR (0°)	205°	-25°	0.2394
with TR (5°)	205°	-25°	0.2365

Figure 14 shows the BVI sound pressure of main-rotor at the position of maximum peak noise level ($\psi=205^\circ$, $\varphi=-25^\circ$) at the distance, $r/R=1000$. Compared with the thickness noise,

the sound pressure waveform of BVI noise clearly shows distinct spikes. The effect of tail-rotor is also not so clear in this main-rotor sound pressure, which makes 3 lines (black, red, and blue) almost identical. The reason of weak effect of tail-rotor can be explained using the sound pressure of tail-rotor in Fig. 15. When main-rotor BVI happens, the peak noise level from main-rotor is considerably high compared to the other noises including tail-rotor interaction noise. Especially the interaction between main-rotor wake and tail-rotor is not so strong owing to the rotating direction and interaction position. As shown in Fig. 15, self interaction noise of tail-rotor is larger than the interaction noise between main-rotor wake and tail-rotor.

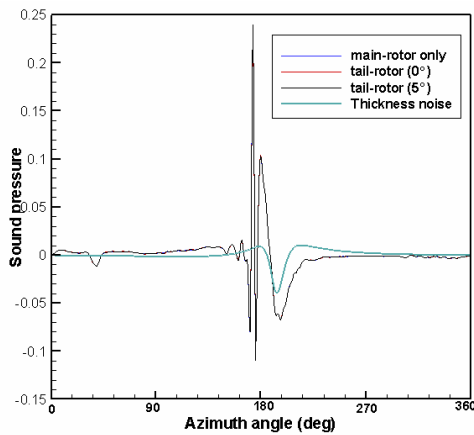


Fig.14: BVI sound pressure of main rotor

At a different observation position, the relative scale between self interaction noise of tail-rotor and the wake interaction noise are shown in Fig. 16. For more general combination of tail-rotor rotation speed and number of blade should be considered at the practical flight condition of helicopter. There are many difficulties in calculating tail-rotor rotation on account of its complicated operating condition and aerodynamic environment as well as the increasing needs of huge computing resource. In special, the difference of rotating speed and the discrepancy of geometry between main-rotor and tail-rotor blades make difficulties in deciding the magnitude of time step. At the next step, various tail rotor parameters such as

rotation speed, rotating direction, location of rotation center, can be considered. Then, to develop full helicopter analysis code, fuselage can be included. More researches are needed in the sensitivity of grid size and time step according to the flight conditions to get more robust solution.

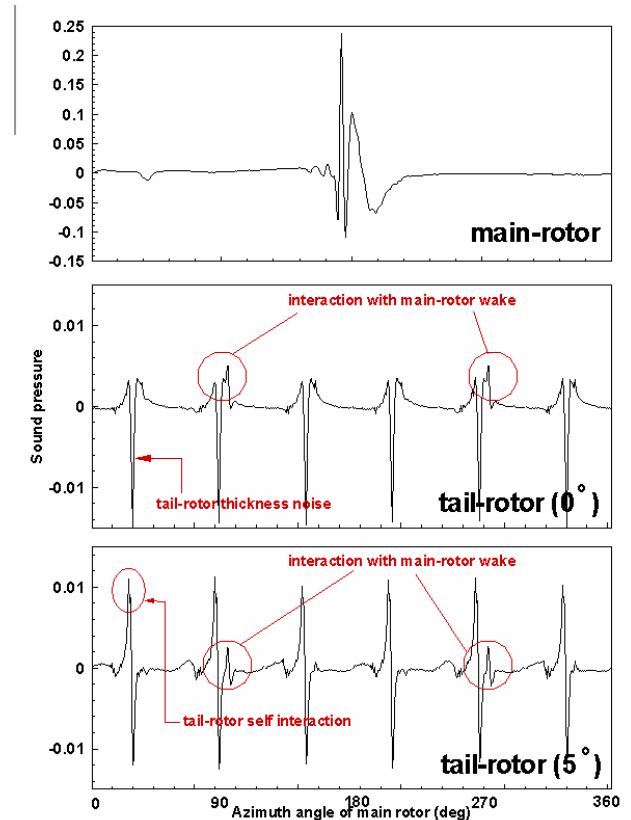


Fig.15: BVI sound pressure of tail-rotor ($\psi=205^\circ$, $\phi=-25^\circ$, $r/R=1000$)

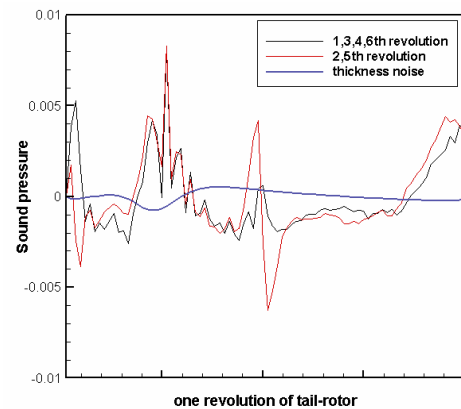


Fig.16: BVI sound pressure of tail-rotor ($\psi=155^\circ$, $\phi=-65^\circ$, $r/R=1000$)

4 Conclusions

Main-rotor and tail-rotor noise are analyzed using a combination method of an unsteady Euler code with an aeroacoustic code based on the Ffowcs-Williams and Hawkings formulation. The effect of tail-rotor onto main-rotor and the tail-rotor noise are calculated for the helicopter operating conditions, and the following conclusions are obtained.

- (1) A moving overlapped grid system with three types of grids is used to simulate BVI of helicopter, and the calculated waveform of BVI noise clearly shows distinct peaks caused by the interactions between blades and tip vortices.
- (2) In hovering flight, the presence of tail-rotor disturbs the surface pressure of main-rotor because the tip vortex of tail-rotor is drawn by the induced flow of main-rotor.
- (3) In forward flight, tail-rotor noise including self interaction noise and interaction noise between tail-rotor and tip vortex of main rotor is well-captured.
- (4) Using hemispherical surface, the directivity of BVI noise is analyzed, but the tail-rotor noise in this flight condition is relatively small compared to the large BVI noise.

References

- [1] White, R. P. Jr., The status of rotor noise technology: One man's opinion, NASA Center for AeroSpace Information (CASI), 1978
- [2] Chou, S. -T., A study of rotor broadband noise mechanism and helicopter tail-rotor noise, NASA-CR-177565, 1990
- [3] Martin, R.M., Acoustic test of a model rotor and tail-rotor: Results for the isolated rotor and combined configuration, NASA-TM-101550, 1989
- [4] Balch, D. T., Lombardi, J., Experimental study of main-rotor tip geometry and tail-rotor interaction in hover. Volume 1. Text and figures, NASA-CR-177336-VOL-1, 1985
- [5] Balch, D. T., Lombardi, J., Experimental study of main-rotor tip geometry and tail-rotor interaction in hover. Volume 2. Run log and tabulated data, NASA-CR-177336-VOL-2, 1985
- [6] George, A. R. and Chou, S. -T., Helicopter tail-rotor blade-vortex interaction noise, NASA-CR-183178, 1987
- [7] George, A. R. and Chou, S. -T., Helicopter tail-rotor noise analysis, NASA-CR-176829, 1986
- [8] Ahmadi, A. R., An experimental investigation of the chopping of helicopter main-rotor tip vortices by the tail-rotor, NASA-CR-177338, 1984
- [9] Leverton, J. W., Pollard, J. S., and Wills, C. R., Main rotor wake/tail rotor interaction, *Vertica*, Vol.1, pp.213-221, 1977
- [10] Boxwell, D.A., Schmitz, F.H., Spletstoesser, W.R. and Schults, K.J., Helicopter model rotor-blade vortex interaction impulsive noise: scalability and parametric variations, *J. of American Helicopter society*, Vol.32, No.1 pp.3-12, 1987
- [11] Ochi, A., Shima, E., Aoyama, T., and Saito, S., A numerical simulation of flow around rotor blades using overlapped grid, *Proceedings of the 15th NAL Symposium on Aircraft Computational Aerodynamics (NAL SP-37)*, pp.211-216, Tokyo, Japan, Jul 1997oacoustics Conference, AIAA 86-1877, 1986
- [12] Roe, P. L., Approximate Riemann solvers, parameter vectors, and difference schemes, *Journal of Computational Physics*, Vol.43, pp. 357-372, 1981
- [13] Aoyama, T., Kawachi, K., Saito, S. and Kamio, J. Unsteady analysis of transonic helicopter rotor noise, 19th European Rotorcraft Forum, 1993
- [14] Yamamoto, S. and Daiguji, H., Higher-order-accurate upwind schemes for solving the compressible Euler and Navier-Stokes equations, *Journal of Computers & Fluids*, 22, pp.259-270, 1993
- [15] Shima, E. and Jounouchi, T., Role of CFD in aeronautical engineering (No.14) -AUSM type upwind schemes-, *Proceedings of the 14th NAL Symposium on Aircraft Computational Aerodynamics (NAL SP-34)*, pp.7-12, Tokyo, Japan, Jul 1996
- [16] Farassat, F., Theory of noise generation from moving bodies with an application to helicopter rotors, NASA TR R 451, 1975
- [17] Brentner, K. S., Helicopter rotor noise prediction: Background, current status, and future direction, Seminar in University Tennessee Space Institute, Chattanooga, Tennessee, 1997
- [18] Johnson, W., Rotorcraft aerodynamics applications of comprehensive analysis, Heli-Japan 98, Paper No.S5, Gifu, Japan, April 1998
- [19] Heyson, Harry H., Linearized Theory of Wind-Tunnel Jet-Boundary Corrections and Ground Effect for VTOLSTOL Aircraft. NASA TR R-124, 1962